International Journal of Environmental Sciences
ISSN: 2229-7359
Vol. 11 No. 21s, 2025
https://www.theaspd.com/ijes.php

Photo Catalytic Activity, Optical, DFT and Spectral (FT-IR, FT-Raman, UV-Visible) Appraisal on

Novel Copper Chloride Modified 3- hydroxy-2-(3-nitrophenyl)-4H-chromen-4-one-TiO_2 Nanoparticles

R. S. Bemina[a], T. Joselin Beaula[b,*], S. R. Gibin[c], Reshma J. S[d]
[a]Reg. No. 22213082132010, Research Scholar, Department of Physics and Research Centre, Malankara Catholic College, Mariagiri-629153, Tamilnadu, India, Affiliated to Manonmaniam Sundaranar University, Abishekapatti-627012, Tirunelveli, Tamilnadu, India.
[b]Assistant Professor, Department of Physics and Research Centre, Malankara Catholic College, Mariagiri-629153, Tamilnadu, India.
[c]Associate Professor of Physics, Sree Sakthi Engineering College (Autonomous), Karamadai, Coimbatore-641104, Tamil Nadu, India (Affiliated to Anna University, Chennai).
[d]Research Scholar, Department of Physics and Research Centre, Malankara Catholic College, Mariagiri-629153, Tamilnadu, India.
*joselinbeaula@gmail.com

Abstract
Copper chloride-modified 3-hydroxy-2-(3-nitrophenyl)-4H-chromen-4-one-TiO_2 (CHT) nano particles were produced using the reflux method. It was structurally examined using a number of analytical and spectroscopic techniques, including Fourier-transform infrared (FT-IR) spectroscopy, FT-Raman spectroscopy, ultraviolet-visible (UV-Vis) spectroscopy, and powder XRD. Furthermore, theoretical research was carried out to investigate the electrical characteristics of CHT. B3PW91/LANL2DZ calculates the molecule's frontier molecular orbital (FMO) and molecular electrostatic potential (MEP) at the theoretical level. The CHT band gap energy was reduced from 3.30 eV (bare TiO_2) to 1.16 eV. UV irradiation was used for the photocatalytic breakdown of Malachite Green dye, which resulted in a higher efficiency.
Keywords: *CHT; FMO; MEP; NLO; Photo-catalytic Dye Degradation*

1. INTRODUCTION

The utilization of hybrid materials has received more attention recently. With their exceptional separation capabilities, strong chemical and thermal stability, ability to form membranes, and tolerance to hostile environments, these materials may combine the basic properties of inorganic and organic materials to provide unique advantages. Organic-inorganic hybrid materials have garnered increased interest as novel membrane materials. Experimental band gaps in TiO_2, anatase, rutile, and brookite range from 3.0 to 3.3 eV, with anatase exhibiting longer lifetimes for photo generated electrons and holes [1]. However, due to its low electron transfer efficiency and crystal flaws, the TiO_2 showed some degree of polarization relaxation [2]. TiO_2 nanoparticles are utilized in various industries, including food, cosmetics, paints, printing ink, plastics, paper, and more. They also have advanced applications in photovoltaic cells and photo catalytic pollution destruction [3]. Metal complexes on TiO_2 surface enhance its photo catalytic activity, acting as functional materials for increased adsorption and photo degradation, and acting as high energy photon sensitizers, thereby enhancing semiconductor photo catalytic activity. Metal complexes, formed by combining metal-organic ligands and TiO_2, have attractive structures, large surface areas, micro porous diameters, and adsorbate-ML interaction sites, with their functional properties determined by their pores. Catenation enhances pore volume, opens metal sites, and incorporates functional groups into metal complexes in an octahedral environment due to the relationship between complex structures and potential characteristics [4].

TiO_2-based solution-processable nanoparticles used for solar-blind deep-UV photodetector [1], Pt nanoparticles adapted α-Fe_2O_3/TiO_2 nanotubes have profitable photo electrochemical water splitting [5], noble (Ag^+, Au^{2+}, Pt^{2+}, Pd^{2+}, and $Ru^{\delta+}$) metal-ion modified TiO_2 rutile nanobars exhibit high activity for H_2 generation from water splitting [6], Thiazolylazopyrimidine-functionalized TiO_2 nanosensor (TiO_2-TAP) was used for selective colorimetric detection and recovery of Cu^{2+} ions [7], surface modification of commercial TiO_2 powder with various phenol derivatives has visible-light-response properties [8]. Under

visible light irradiation, both bare and Fe-modified TiO_2 exhibit simultaneous oxidation of NO and acetaldehyde [9], surface alteration of TiO_2 with a affordable metal (iron) demonstrates breakdown of tryptophan molecules via photo catalysis [10], surface improved nanoparticles of P25 Evonic Degussa TiO_2 with silane coupling compound 3-(2-aminoethylamino) propyltrimethoxysilane possess photoconductivity [11]. Surface plasmonic Bi nanoparticles and α-Bi_2O_3 co-modified TiO_2 nanotube arrays were employed for broadened photo catalytic destruction of ciprofloxacin [12], TiO_2 thin films tweaked with Anderson-type polyoxometalates (Cr, Co, and Ni) exhibit photo catalytic degradation of MB colorant [13], For photo catalytic CO_2 reduction hollow cubic TiO_2 filled with copper and gold nanoparticles were used [14], 4-chlorophenol -modified TiO_2 powder exhibits visible-light-response [15]. Malachite green dye was degraded using a novel nanocatalyst nitrogen/sodium/iron- doped TiO_2 [16], when exposed to UV and visible light, Ag-coated Nd-doped TiO_2 nanoparticles can degrade methylene blue dye [17], the NO_2 and N_2O adsorption effectiveness was increased by modifying TiO2 surface with transition metals (M=Cu, Fe, and Mn) [18]. Under UV light irradiation, the Cu@TiO_2@SAPO-34 nanocomposite is utilized for photo catalytic mortification of organic contaminants, aqueous methylene blue dye degradation, actual waste water treatment, and coated surface cleaning [19], high mercury oxidation activity is exhibited by Ru, Nb, Mo, and Mn modification on Ce/TiO_2 catalyst [20].

Flavonols are a significant part of the flavonoid family found in various plants such as fruits, vegetables, cereals, and aquatic ones [21]. Flavonols are studied for metal ion detection and are considered ideal fluorophores for creating fluorescent probes. Free radicals, reactive oxygen species, and reactive nitrogen species are naturally present in healthy organisms and play a role in metabolic processes. Excessive levels of these chemicals can damage cells and cause illnesses like cancer, atherosclerosis, and heart conditions [22]. Copper, a crucial trace element for metabolism, antioxidant defense, angiogenesis, and tissue growth, is essential for normal physiological conditions. However, excessive copper consumption can lead to health issues like Menkes, Parkinson's, Wilson's, and Alzheimer's. Copper is primarily found in soil and aquatic habitats as Cu^{2+} [23]. Flavonoids can bind iron and copper, reducing transition metal ions and making metal ions inactive in producing radicals. They may also absorb the radicals produced, making flavonoids potentially crucial in metal-overload disorders like hemochromatosis and Wilson's disease, due to their metal chelating properties. This study examines the structural characteristics, functional group interpretation, electronic properties, reactive site exploration and the photo degradation of organic contaminant such as malachite green dye using produced novel photo catalyst copper chloride modified 3-hydroxy-2-(3-nitrophenyl)-4H-chromen-4-one-TiO2 nanoparticles.

2. MATERIALS AND METHODS

2.1 Synthesis and Growth of CHT

The synthesis was done on basis of the procedure explained by S. Rajendran et al [4]. Initially, 4-nitrobenzaldehyde and 1-(2-hydroxyphenyl) ethanone were reacted in equal proportions to produce a chalcone. The resulting chalcone was separated by precipitation after cooling after the reactants were refluxed under a water bath until the process was finished. A flavonol was then produced by an oxidative modification of the chalcone. The chalcone was treated with a 30% H_2O_2 and NaOH solution to accomplish this conversion. After filtration, the precipitated flavonol was gathered, thoroughly cleaned with ethyl acetate, and dried.

The produced flavonol was then used as a ligand to create a metal complex, a molar ratio of 1:2; a methanolic solution containing 0.61 g (2 mM) of the flavonol was gradually added, while being constantly stirred, to a methanolic solution containing 0.24 g (1 mM) of $CuCl_2$ $2H_2O$. As soon as the ligand was added, the color of the solution changed to brown. After stirring for 24 hours at room temperature, a brown precipitate developed. After being separated, this precipitate was carefully cleaned with hexane and vacuum-dried.

Three grams of titanium dioxide (TiO_2) and 0.1 grams of the manufactured metal complex were dissolved in 50 ml of chloroform to create a suspension combination of metal ligand and TiO_2. After being moved to a round-bottom flask with a reflux condenser, this mixture was refluxed for three hours at 70°C. The mixture was cooled after reflux, and the solid composite was filtered out. Extensive washing was

performed to remove unreacted metal complexes, and the metal ligand - TiO_2 composite was dried for an hour at 100°C in an oven.

2.2 Photocatalytic Degradation

The photodegradation of the dye Malachite green (MG) in Pyrex glass tubes under UV light illumination was used to measure the photocatalytic activity of CHT. Following specific time periods, the dye solutions were examined with a UV-visible spectrophotometer in the 200-900 nm range to determine the degree of dye degradation, which is connected to the values of the Malachite green λ_{max}, which is 662 nm. To ascertain the catalysts' capabilities, the blank dye solution devoid of the catalysts was also examined as needed. The degradation process of MG is indicated by the change in absorbance of MG dye over time. The Beer-Lambert relation was used to plot the photocatalytic activity values, and the following formula was used to get the dye degradation percentage:

$$\% \text{ degradation} = \frac{A0-At}{A0} \times 100 = \frac{C0-Ct}{C0} \times 100 \quad (1)$$

where C_0 is the dye's initial concentration and C_t is its final concentration, and A_0 and A_t are the MG absorbance at the initial and final stages, respectively.

2.3 Experimental and Computational Details

Powder X-ray diffraction (XRD) measurements were performed on a Bruker D2 PHASER instrument, utilizing Cu-Kα radiation at a wavelength of λ=1.5406 Å. Fourier-transform infrared (FT-IR) spectra were acquired in the 4000-400 cm^{-1} range using an IR Prestige-21 spectrometer. For FT-Raman spectroscopy, a Bruker RFS 27 standalone spectrometer was employed, featuring a 1064 nm Nd:YAG laser source and a spectral resolution of 2.0 cm^{-1} over the 4000-50 cm^{-1} range. The UV-visible absorption spectra of the solid material were investigated using a ThermoFisher Evolution 220 UV/VIS/NIR spectrometer. Gaussian'09W software [24] was utilized for quantum chemical calculations of CHT at the DFT level of B3PW91/LANL2DZ, while Gauss View 5.0 [25] was utilized for optimizing the molecule, computing vibrational assignments, HOMO-LUMO and for plotting MEP.

3. RESULTS AND DISCUSSION

3.1 Powder XRD Peak Indexing

Powder XRD analyses were performed on the sample to determine the values of the unit cell and structural organization, so that distinct and sharp Bragg's peaks verified that CHT is crystalline. Table 1 gives the values, and Fig. 1 shows the peak indexing using Miller indices.

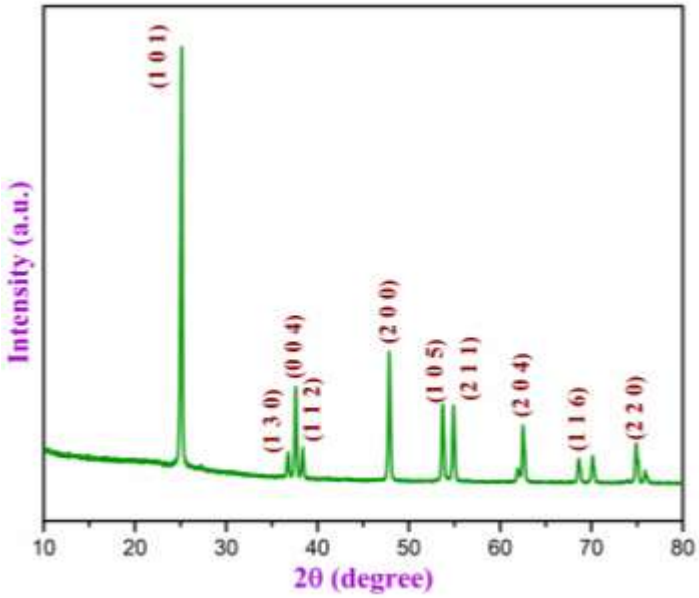

Fig. 1 PXRD peak illustration of CHT

The successful observation of the anatase TiO_2 crystal planes (1 0 1), (0 0 4), (2 0 0), (1 0 5), and (2 1 1) was in accordance with the standard card (PDF #73-1764). $CuCl_2$ peak 36.79° (1 3 0) shifted to higher

intensity [26] and the peak at 74.89° (2 2 0) shows the presence of Cu inside the MOF. The peak shifting is due to the incorporation of the organic compound.

Table 1 PXRD parameters of CHT

2θ (°)	h	k	l
25.09	1	0	1
36.79	1	3	0
37.61	0	0	4
38.38	1	1	2
47.83	2	0	0
53.67	1	0	5
54.89	2	1	1
62.49	2	0	4
70.11	1	1	6
74.89	2	2	0

3.2 Geometrical Structure Exploration

The DFT/B3PW91 approach was used to optimize the molecular structure using the LANL2DZ basis set in order to anticipate the best optimal structure of the NHT molecule. Fig. 2 displayed the labeled molecule's structures. The NHT's computed molecular geometry parameters, including bond length, bond angle, and dihedral angle, are displayed in Table 2. The bond angles of C15-C14-C16 (119.27°), C15-C17-C21 (119.11°), and C16-C19-C21 (118.79°) are compressed, and C17-C21-C19 (121.88°) is elongated than usual C-C-C (~120°) bond angles due to the substitution of nitro (-NO_2) group in the para-nitrophenyl moiety. Additionally, the predicted bond distances of C14-C15 (1.4183 Å), C14-C16 (1.4183 Å), C17-C21 (1.4017 Å), and C19-C21 (1.4038 Å) have been extended in comparison to other C-C (~1.39 Å) bond distances in the nitrophenyl ring [27].

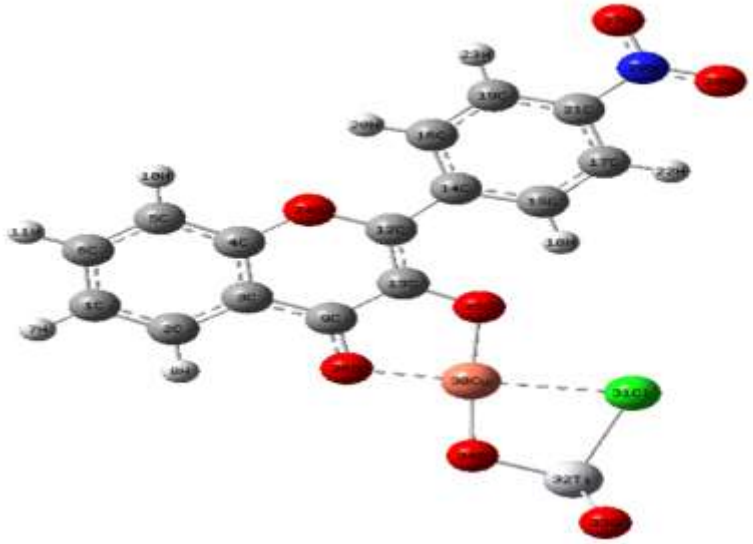

Fig. 2 optimized geometry representation of CHT

C-O bond lengths are given by C4-O24 (1.3786 Å), C12-O24 (1.3914 Å), C13-O25 (1.3482 Å) and C9-O26 (1.3049 Å). The remaining bonds are all single, with the exception of the double bond C9-O26 (1.3049 Å). A deprotonated group is often predicted by a difference of ≤ 0.03 Å, whereas a protonated group is predicted by a difference of ≥ 0.08 Å in the C-O bonds [28]. The C15-H18...O25 hydrogen bonding interaction between the benzopyran and para nitro phenyl moieties occurs at a distance of 2.0858 Å. The typical single C-N bond length of 1.480 Å is about equivalent to the C-N bond length C21-N29 (1.4698 Å) [29]. The use of a NO_2 group replaces the hydrogen atom in a structure, causing a decrease in electron density at the ring carbon atom, and fall in the bond length.

Due to the presence of an electronegative chlorine atom, the Cu-O bond lengths in were longer than the typical range (1.73-1.79 Å) [30] and Ti-O bond lengths were decreased (1.83-2.09 Å) [31]. These are provided by Cu30-O25 (1.8974 Å), Cu30-O26 (1.9914 Å), Cu30-O33 (4.2476 Å), Cu30-O34 (1.9093 Å)

Ti32-O33 (1.6318 Å) and Ti32-O34 (1.7289 Å). The longest bond length inside the CHT molecule is 4.2476 Å, which is the interaction bond between Cu30 and O33. According to calculations, the M-Cl bond length is 2.6068 Å for Cu-Cl and 2.3951 Å for Ti-Cl [32].

Table 2 Geometrical parameters of CHT

Bond Length	Value (Å)	Bond Angle	Value (°)	Dihedral Angle	Value (°)
C1-C2	1.3898	C2-C1-C6	120.1935	C6-C1-C2-C3	0.0123
C1-C6	1.4197	C2-C1-H7	120.1716	C6-C1-C2-H8	179.8646
C1-H7	1.0854	C6-C1-H7	119.6348	H7-C1-C2-C3	-179.9087
C2-C3	1.4181	C1-C2-C3	119.8332	H7-C1-C2-C8	-0.0564
C2-H8	1.0853	C1-C2-H8	121.8819	C2-C1-C6-C5	-0.0325
C3-C4	1.4149	C3-C2-H8	118.2847	C2-C1-C6-H11	-179.9791
C3-C9	1.436	C2-C3-C4	118.9796	H7-C1-C6-C5	179.889
C4-C5	1.4045	C2-C3-C9	123.315	H7-C1-C6-H11	-0.0576
C4-O24	1.3786	C4-C3-C9	117.7053	C1-C2-C3-C4	0.0359
C5-C6	1.3943	C3-C4-C5	121.5198	C1-C2-C3-C9	179.9033
C5-H10	1.0846	C3-C4-O24	121.0342	H8-C2-C3-C4	-179.8217
C6-H11	1.0861	C5-C4-O24	117.4459	H8-C2-C3-C9	0.0457
C9-C13	1.4485	C4-C5-C6	118.4854	C2-C3-C4-C5	-0.0666
C9-O26	1.3049	C4-C5-H10	119.5334	C2-C3-C4-O24	179.9528
C12-C13	1.394	C6-C5-H10	121.9812	C9-C3-C4-C5	-179.9414
C12-C14	1.4578	C1-C6-C5	120.9884	C9-C3-C4-O24	0.078
C12-O24	1.3914	C1-C6-H11	119.6055	C2-C3-C9-C13	-179.448
C13-O25	1.3482	C5-C6-H11	119.4061	C2-C3-C9-O26	0.5907
C14-C15	1.4183	C3-C9-C13	119.6833	C4-C3-C9-C13	0.421
C14-C16	1.4183	C3-C9-O26	123.4635	C4-C3-C9-O26	-179.5404
C15-C17	1.397	C13-C9-O26	116.8532	C3-C4-C5-C6	0.0469
C15-H18	1.0838	C13-C12-O24	127.5262	C3-C4-C5-H10	179.9887
C16-C19	1.3938	C13-C12-O24	119.1277	O24-C4-C5-C6	-179.9718
C16-H20	1.0842	C14-C12-O24	113.3461	O24-C4-C5-H10	-0.03
C17-C21	1.4017	C9-C13-C12	119.9488	C3-C4-O24-C12	-0.2941
C17-H22	1.084	C9-C13-O25	115.3455	C5-C4-O24-C12	179.7246
H18-O25	2.0858	C12-C13-O25	124.7054	C4-C5-C6-C1	0.0029
C19-C21	1.4038	C12-C14-C15	120.6682	C4-C5-C6-H11	179.9496
C19-H23	1.084	C12-C14-C16	120.0559	H10-C5-C6-C1	-179.9374
C21-N29	1.4698	C15-C14-C16	119.2758	H10-C5-C6-H11	0.0093
O25-Cu30	1.8974	C14-C15-H17	120.2492	C3-C9-C13-C12	-0.7288
O26-Cu30	1.9914	C14-C15-H18	119.062	C3-C9-C13-O25	179.4804
O27-N29	1.2744	C17-C15-H18	120.6887	O26-C9-C13-C12	179.235
O28-N29	1.2732	C14-C16-C19	120.6744	O26-C9-C13-O25	-0.5557
Cu30-Cl31	2.6068	C14-C16-H20	119.4993	C3-C9-26-Cu30	-178.7779
Cu30-O33	4.2476	C19-C16-H20	119.8263	C13-C9-26-Cu30	1.2597
Cu30-O34	1.9093	C15-C17-C21	119.1178	C14-C12-C13-C9	-179.3824
Cl31-Ti32	2.3951	C15-C17-H22	121.1535	C14-C12-C13-O25	0.3876
Cl31-O33	3.5604	C21-C17-H22	119.7287	O24-C12-C13-C9	0.5222
Cl31-O34	3.0232	C16-C19-C21	118.7944	O24-C12-C13-O25	-179.7078
Ti32-O33	1.6318	C16-C19-H23	121.6171	C13-C12-C14-C15	-0.366
Ti32-O34	1.7289	C21-C19-H23	119.5884	C13-C12-C14-C16	179.522
		C17-C21-C19	121.8882	O24-C12-C14-C15	179.7248
		C17-C21-N29	119.2054	O24-C12-C14-C16	-0.3872
		C19-C21-N29	118.9064	C13-C12-O24-C4	-0.0151

		C4-O24-C12	122.497	C14-C12-O24-C4	179.9025
		C13-O25-Cu30	112.7349	C9-C13-O25-Cu30	-0.507
		C9-O26-Cu30	110.5504	C12-C13-O25-Cu30	179.7135
		C21-N29-O27	118.0326	C12-C14-C15-C17	179.7873
		C21-N29-O28	118.1615	C12-C14-C15-H18	-0.223
		O27-N29-O28	123.8059	C16-C14-C15-C17	-0.1015
		O25-Cu30-O26	84.4986	C16-C14-C15-H18	179.8881
		O25-Cu30-Cl31	93.3032	C12-C14-C16-C19	-179.7988
		O25-Cu30-O33	143.7928	C12-C14-C16-H20	0.1606
		O26-Cu30-Cl31	175.1572	C15-C14-C16-C19	0.0908
		O26-Cu30-O34	99.9485	C15-C14-C16-H20	-179.9498
		O33-Cu30-O34	30.854	C14-C15-C17-C21	0.0213
		O33-Cl31-O34	49.2471	C14-C15-C17-H22	179.9944
		O33-Ti32-O34	111.975	H18-C15-C17-C21	-179.9682
		Cu30-O33-Ti32	32.4159	H18-C15-C17-H22	0.0049
		Cu30-O34-Ti32	111.0199	C14-C16-C19-C21	0.0002
				C14-C16-C19-H23	179.9726
				H20-C16-C19-C21	-179.959
				H20-C16-C19-H23	0.0134
				C15-C17-C21-C19	0.0729
				C15-C17-C21-N29	-179.9208
				H22-C17-C21-C19	-179.9005
				H22-C17-C21-N29	0.1057
				C16-C19-C21-C17	-0.0837
				C16-C19-C21-N29	179.9101
				H23-C19-C21-C17	179.9433
				H23-C19-C21-N29	-0.0629
				C17-C21-N29-O27	-179.8919
				C17-C21-N29-O28	0.1439
				C19-C21-N29-O27	0.1141
				C19-C21-N29-O28	-179.8501
				C13-O25-Cu30-O26	0.9249
				C13-O25-Cu30-Cl31	176.5967
				C13-O25-Cu30-O33	-151.8706
				C13-O25-O34-Ti32	175.9367
				C9-O26-Cu30-O25	-1.214
				C9-O26-Cu30-Cl31	-64.3994
				C9-O26-Cu30-O34	175.69
				C9-O26-O33-Ti32	-81.2817
				O25-Cu30-O33-Ti32	-99.7198
				O34-Cu30-O33-Ti32	81.5986
				O26-Cu30-O34-Ti32	174.0948
				O33-Cu30-O34-Ti32	-32.426
				O34-Ti32-O33-Cu30	-37.1708
				O33-Ti32-O34-Cu30	129.4746

3.3 Vibrational Assignments

The FT-IR and FT-Raman spectra of CHT, both theoretical and experimental, were presented in Figure 3. Table 3 provided a detailed analysis of the vibrational wave numbers of CHT for various functional groups.

3.3.1 C-C, C=C, and C-H vibration

For CHT, the C-C stretching vibration was detected between 1120 and 1055 cm^{-1}. The C-C stretching vibration is represented by the medium and weak bands in the FT-IR and FT-Raman spectra that are observed at 1117 and 1111 cm^{-1}. Delocalization of π electrons in the benzopyran ring caused the variation in C-C stretching vibration. It was anticipated that the benzene ring's C-H stretching vibration would fall between 3100 and 3000 cm-1 [33]. Eight bands for CHT correspond to the stretching vibration of C-H. The C-H stretching vibration is represented by the faint bands observed at 3240, 3262, and 3282 cm^{-1} in the FT-IR and 3236, 3259, and 3273 cm^{-1} in the FT-Raman spectrum. At 3236, 3250, 3261, 3263, 3264, 3270, 3278, and 3282 cm^{-1}, the calculated values were recorded. It was predicted that the C-H in-plane bending vibration would be at 1300 to 1000 cm^{-1}. C-H in-plane bending vibration is represented by the bands observed at 1140, 1200, 1219, and 1238 cm^{-1} in the FT-IR spectra and at 1136, 1207, and 1321 cm^{-1} in the FT-Raman spectrum. 1057, 1147, 1201, 1220, 1237, and 1343 cm^{-1} was the computed values.

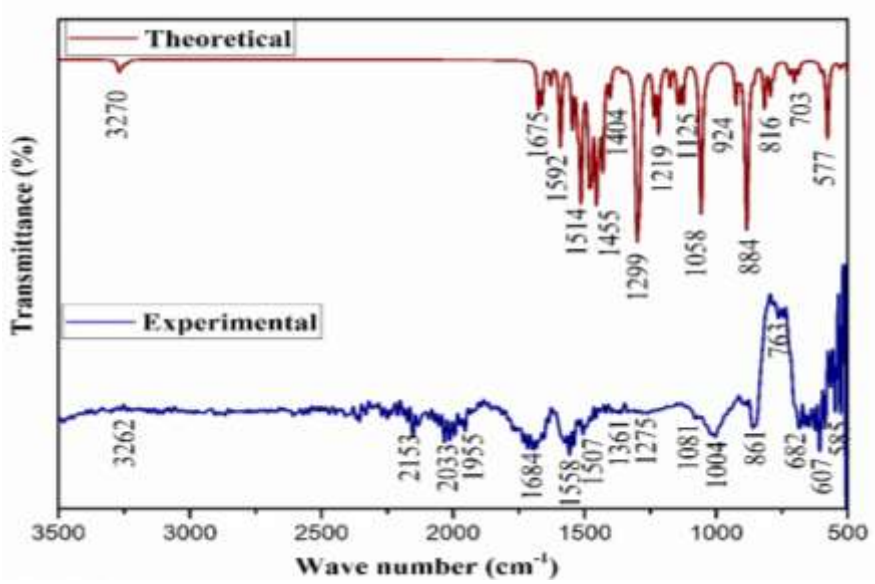

Fig. 3 Theoretical and experimental FT-IR spectra of CHT

3.3.2 C-N, C-O and C=O vibration

C-N stretching frequencies typically range from 1450-950 cm^{-1} [34], in CHT very strong band at 1299 cm^{-1} in FT-IR spectra, computed at 1293 cm^{-1} with a 13% PED contribution. The absorption of the carbonyl group can be triggered by both carbon and oxygen atoms due to their shared vibrational frequency C-O stretching is found between 1260 and 1000 cm^{-1} [35]. The C-O stretching vibration in this investigation is located from 1267 to 1125 cm^{-1}. Because of their proximity, other vibrations force the C-O vibration to the lower region. The C=O stretching vibrations [36] are predicted to occur in the region 1715-1680 cm-1. In the current work, this mode shows at 1474 cm^{-1} in the infrared spectrum, the red shift (~206) observed is due to the presence of metal chloride attachment.

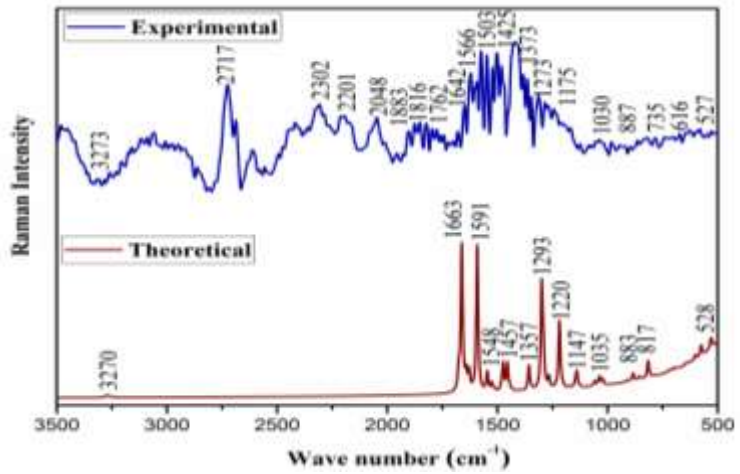

Fig. 4 Experimental and theoretical FT-Raman spectra of CHT

3.3.3 Nitro group vibration

The asymmetric and symmetric stretching vibrations of the NO_2 group at the 1570-1485 and 1370-1320 cm^{-1} region, respectively, give aromatic nitro compounds their significant absorption. The NO_2 asymmetric stretching vibrations are not significantly affected by hydrogen bonding [37]. The asymmetric NO_2 stretching vibration of the CHT molecule is identified by the strong bands at 1566 cm^{-1} in the raman spectrum and the weak band at 1558 cm^{-1} in the infrared spectrum; the corresponding calculated value for the NO_2 asymmetric stretching mode is 1548 cm^{-1}. The Raman spectrum's extremely faint band at 1327 cm^{-1} is attributed to the NO_2 symmetric stretching vibration, and 1327 cm^{-1} is the computed value for the NO_2 symmetric stretching mode. Rocking, wagging, and scissoring are some of the normal modes in the vicinity of low frequencies that are affected by the deformation vibrations of the NO_2 group. The rocking mode NO_2 is active at 540 ±70 cm^{-1} for aromatic nitro compounds [37]. In FT-Raman, the wagging mode NO_2 is present at 730 cm^{-1} with a PED contribution of less than 10% and is assigned to aromatic molecules at 740 ± 50 cm^{-1}. According to Table 3, NO_2 rocking vibration is represented by the weak band in the infrared spectrum at 527 cm^{-1}, whereas the theoretically calculated value for the NO_2 rocking mode is 528 cm^{-1}. NO_2 torsion modes are observed in the low wave number range, with theoretically occurring vibrations around at 64 cm^{-1}.

Table 3 Vibrational assignments of CHT by NCA based on SQMFF calculations

Wave numbers (cm^{-1})			Assignment with PED (> 10%)
Obs.		Cal.	
FT-IR	FT-Raman		
3282		3282	νCH (94)
		3278	νCH (97)
	3273	3270	νCH (99)
		3264	νCH (84), R δ_{as} (10)
		3263	νCH (99)
3262		3261	νCH (92)
	3259	3250	νCH (99)
3240	3236	3236	νCH (99)
1671		1677	R δ_{as} (57), R δ'_{as} (16), νCC (13), R δ_t (11)
		1663	R δ'_{as} (40), R δ_{as} (40), νCC (16)
1654		1642	νCC (47), R δ_{as} (25), R δ'_{as} (19)
1636	1628	1629	νCC (59), R δ_{as} (25)
	1609	1591	R δ_{as} (40), νCC (39)
1558	1566	1548	R δ_{as} (32), νCC (21), R δ'_{as} (20), ν_{as}NO (15)
1541	1543	1543	R δ_{as} (47), νCC (19), R δ'_{as} (16)
1520		1522	R δ_{as} (43), νCC (22), R δ_t (16), βCH (13)
1507	1503	1513	R δ_{as} (59), R δ'_{as} (22)
1474		1475	R δ_t (45), νCC (20), βCH (16), νC=O (13)
1457	1456	1457	R δ'_{as} (28), R δ_t (25), νCC (21), βCH (10)
		1445	R δ'_{as} (30), R δ_t (26), νCC (25)
1436		1431	νCC (75), R δ_{as} (11)
1418	1412	1405	νCC (76), R δ'_{as} (10)
1361	1373	1357	R δ_{as} (46), R δ_t (40)
		1343	βCH (47), R δ_t (25),
1317	1327	1327	ν_{ss}NO (57), δ_s NO (11)
1299		1293	R δ_{as} (42), R δ'_{as} (24), R δ_t (11)
1275	1273	1267	R δ_{as} (35), R δ_t (23), νCC (16), νCO (13)
1238	1231	1237	νCO (29), βCH (25), R δ_t (17), νCC (14)
1219		1220	R δ_{as} (38), R δ_t (18), βCH (18), νCO (10)
1200	1207	1201	βCH (72), νCC (15)
1178	1175	1174	R δ_{as} (52), νCO (13), R δ_t (12)

1140	1136	1147	βCH (30), R δ_{as} (29), νCC (20)
1117		1125	R δ_{as} (27), R δ_{t} (26), νCO (14), νCC (12)
	1111	1107	R δ_{as} (38), R δ_{t} (32), νCC (15)
1064		1065	PU (45), R τ'_{as} (29), ω 1 (19)
		1057	νCC (36), R δ'_{as} (17), R δ_{as} (16), βCH (14)
	1051	1050	νTiO (97)
		1045	PU (42), R τ'_{as} (41), ω 1 (16)
		1043	ω 1 (70), R τ_{as} (14), R τ'_{as} (13)
1039	1030	1035	R δ_{t} (70), R δ_{as} (23)
1020		1020	R δ_{t} (45), R δ_{as} (36), R δ'_{as} (10)
1004		1016	R τ_{as} (43), R τ'_{as} (33), ω 1 (22)
923		925	ω 1 (45), PU (39)
		915	PU (43), R τ'_{as} (38), ω 1 (18)
		905	R δ_{t} (47), R δ_{as} (33)
898		894	ω 1 (76), PU (17)
884	887	883	νTiO (75)
859	858	854	R δ'_{as} (43), R δ_{t} (19), R δ_{as} (17), νCC (13)
		817	R τ'_{as} (62), PU (24)
		803	R δ_{as} (53), R δ_{t} (17), R δ'_{as} (16)
		794	R τ'_{as} (49), PU (45)
783		783	R τ'_{as} (49), PU (46)
745	735	745	R δ_{t} (53), R δ_{as} (28)
		727	R τ'_{as} (48), PU (48)
		703	PU (49), R τ'_{as} (36)
		700	R δ'_{as} (52), R δ_{as} (36)
682		687	R δ_{as} (43), R δ'_{as} (25)
646		645	R δ_{as} (62), R δ'_{as} (37)
624	635	627	R τ_{as} (40), PU (32), R τ'_{as} (18)
607	616	618	R δ_{as} (50), R δ_{t} (30)
585		598	R δ_{as} (67), R δ'_{as} (23)
565		545	R δ_{as} (45), R δ'_{as} (20), R δ_{t} (13)
546		544	PU (47), R τ'_{as} (27), R τ_{as} (23)
527	527	528	R δ_{as} (30), rNO (25), R δ'_{as} (18)
	513	522	R δ_{as} (44), R δ'_{as} (23), R δ_{t} (11)
		498	R τ_{as} (45), R τ'_{as} (27), PU (21)
		469	R δ_{as} (54), R δ'_{as} (39)
		448	R τ_{as} (43), R τ'_{as} (41), PU (14)
		438	R δ'_{as} (57), R δ_{as} (18), R δ_{t} (11)
		429	PU (52), R τ'_{as} (26), R τ_{as} (21)
		409	R δ_{as} (45), R δ'_{as} (40)
	396	380	R τ'_{as} (46), R τ_{as} (39)
		338	R δ_{as} (49), R δ'_{as} (31)
		328	νTiCl (40), δ TiO (17), R δ_{as} (11)
		310	R τ_{as} (62), PU (21), R τ'_{as} (15)
		281	R δ_{as} (32), R δ'_{as} (31)
		257	τ 4 (23), ωTiO (16), τ 3 (15)
		246	R τ'_{as} (50), R τ_{as} (36)
	232	230	R δ'_{as} (43), R δ_{as} (35)
		205	τ 4 (33), τ 3 (32), R τ'_{as} (12), PU (11)
	207	201	τ 3 (30), τ 4 (29), R τ'_{as} (10)

		162	τ 3 (27), τ 4 (25), R δ_{as} (16)
		150	R τ'_{as} (35), τ 3 (20), τ 4 (20), PU (15)
	147	144	βCuOTi (24), rTiCl (11), R τ'_{as} (10), δ TiO (10)
		123	R τ'_{as} (55), R τ_{as} (19)
		106	R τ'_{as} (50), R τ_{as} (45)
		100	PU (37), R τ'_{as} (25)
		93	βCuOTi (32), τ 3 (13), τ 4 (13)
		79	τ 3 (41), τ 4 (33)
		70	τ 4 (39), τ 3 (33)
		64	τ 1 (37), PU (26), R τ'_{as} (21), R τ_{as} (15)
		41	τ 3 (37), τ 4 (28), PU (18)
		35	τ 3 (45), τ 4 (40)
		27	τ 3 (38), PU (20), R τ_{as} (12)
		20	τ 4 (56), τ 3 (41)

vs: very strong, s: strong, m:medium, vw: very weak, w: weak, ν:stretching, β: bending; ω: wagging, r: rocking, τ: torsion, ν_{ss}: symmetric stretching, ν_{as}: asymmetric stretching, δ: deformation, δ_s: symmetric deformation, δ_{as}: asymmetric deformation, δ'_{as}: asymmetric deformation out of plane, δ_t: trigonal deformation, τ: torsion, τ_{as}: asymmetric torsion, τ'_{as}: asymmetric torsion out of plane, PU: puckering, R: ring.

3.3.4 Cu-O, Ti-O, Ti-Cl vibration

The normal range of Cu-O stretching vibrations is 400-700 cm^{-1}. The bending mode in CHT is at 256 cm^{-1}, and it is also present at 443 and 575 cm^{-1}. Low frequency vibrations of metal oxide and metal choride were observed. Ti-O vibration is indicated by peaks in the 400-1000 cm^{-1} range, while in CHT, it is found at 1051 and 883 cm^{-1}. The TiO_2 nanoparticle exhibits wagging at 257 cm^{-1} and deformation at 328 and 144 cm^{-1}.

3.4 Band Gap Evaluation

3.4.1 UV-Visible Spectra

Fig. 5 describes the UV-visible spectra of CHT in methanol as a solvent. In the UV-visible spectrum, flavonols show two main absorption bands: band I, which is at 372 nm and represents B-ring absorption, and band II, which is at 256 nm and is thought to be connected to the absorption involving the A ring benzoyl system [38]. The blue shift in the bands of CHT at 341 nm is due to the nitro group joining the B-ring (phenyl) of the CHT molecule.

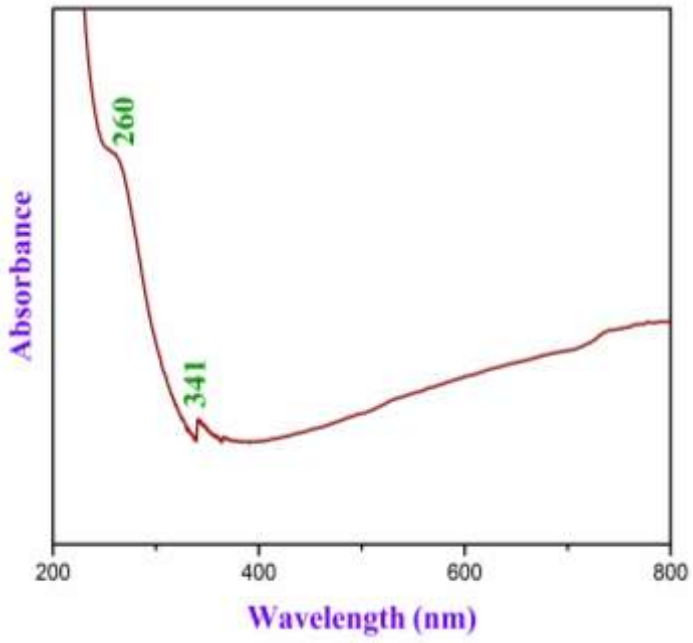

Fig. 5 UV-Visible plot of CHT

3.4.2 Frontier Molecular Orbital Scrutiny

In order to determine the excitation energy and investigate a molecule's reactivity, HOMO-LUMO analysis is crucial [39]. The DFT approach of the CHT reveals differences in energy values, while Table 4 shows theoretically estimated HOMO-LUMO and global reactivity characteristics. These molecular frontier orbitals are crucial in electronic, electric, optical, and quantum chemistry [40], and their clear graphic is shown in Fig. 6. E_{HOMO} and E_{LUMO} estimate electronegativity, chemical hardness, chemical potential, and softness, with chemical hardness indicating a compound's chemical stability as the energy gap value increases with molecular hardness.

In CHT, HOMO is restricted over benzopyran and nitrophenyl groups, while LUMO is restricted over metal chloride and TiO_2. Electrons spread their electron density and transfer their charge as they go from the anion ring to the metal chloride-TiO_2 cation. The molecule's electrophilicity index (ω) determines its classification as either electrophile or nucleophile, with a higher ω value indicating greater electrophilicity. The HOMO-LUMO analysis indicates that the CHT molecule has a high electrophilicity index value of 46.11 eV.

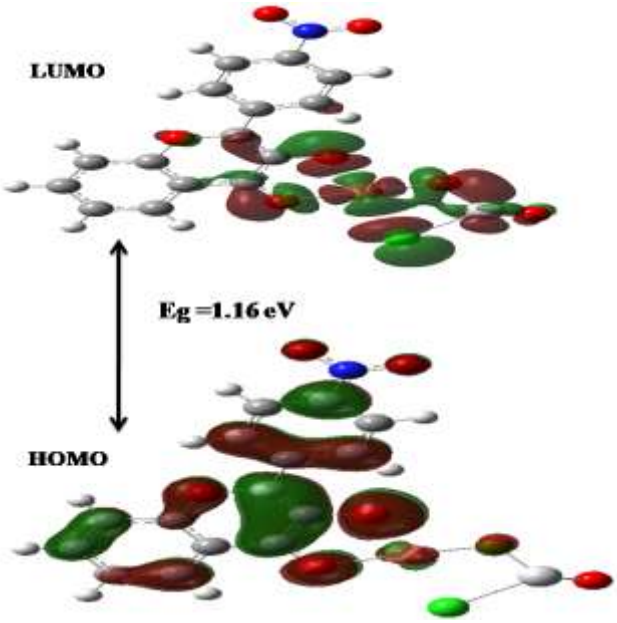

Fig. 6 HOMO-LUMO plot for CHT

The initial inclination of an electron from a stable structure, or ionization potential, is approximately 7.91 eV and signifies that the stability does not break down. Because it can readily donate electrons to an acceptor, a soft molecule with a small energy gap is more reactive than a hard one. The CHT molecule is highly reactive due to extreme polarization caused by its remarkable hardness value of 0.58 eV and its lower softness value of 0.366 eV. Besides the electrophilicity index, the electronegativity of 7.33 eV is widely employed to predict chemical behaviour. The energy reduction caused by the maximum electron flow between the donor and acceptor is measured at 1.16 eV [40].

Table 4 Global reactivity parameters of CHT

Parameter	Value
E_{HOMO} (eV)	-7.91
E_{LUMO} (eV)	-6.75
E_{LUMO} - E_{HOMO} (eV)	1.16
Ionization Potential, I (eV)	7.91
Electron Affinity, A (eV)	6.75
Electronegativity, χ (eV)	7.33
Global Hardness, η (eV)	0.58
Global Softness, σ (eV^{-1})	1.71
Chemical Potential, μ (eV)	-7.33
Electrophilicity Index, ω (eV)	46.11

3.5 Reactive Site Exploration

3.5.1 Molecular Electrostatic Potential Analysis

The molecular electrostatic potential (MEP) is a quantum chemistry technique used to study molecule and living organism behavior, identifying molecular makeup of physiochemical trait correlations in materials, electrophilic assault sites, hydrogen-bonding interactions, and nucleophilic processes [41]. The electron density in CHT is found to be between -2.238×10^{-2} and $+2.238 \times 10^{-2}$. MEP's red regions are associated with electrophilic reactivity (electron-rich zone), whereas it's blue sections are associated with nucleophilic reactivity (electron-deficient region) and green zero potential.

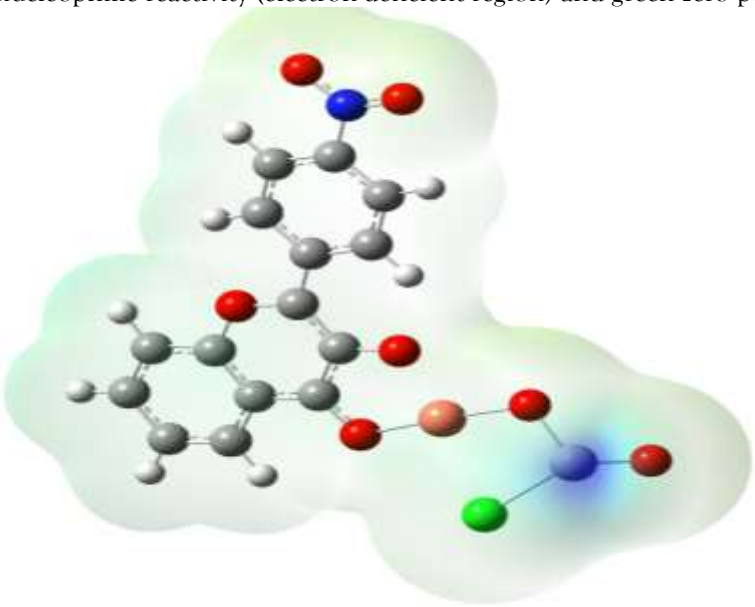

Fig. 7 MEP plot of CHT

MEP studies produce a stable charge surface map for various CHT phases, primarily used for color coding to identify the size, shape, and reactive regions of the head-line molecule [42]. The greatest amount of charge delocalization that occurred in the carbon atoms is indicated by the pale green color of the center section of the benzopyran and phenyl ring. Intramolecular hydrogen bonding interaction C15-H18...O25 was denoted by white potential. Because the oxygen atoms in CHT molecule have a higher electronegativity and act as a nucleophilic area, the TiO_2 with chlorine atom has a bigger electron deficit than other hydrogen atoms. The electron-rich electrophilic region is visible in the pale yellow band encircling the nitro group.

3.6 Optical Characteristics

3.6.1 Non Linear Optical Properties

The use of nonlinear optical characteristics in new organic materials has expanded because of its photonic uses. It happens when radiation interacts with matter particles, producing a new radiation with a different phase, frequency, and amplitude from the incident radiation [43]. It is useful to determine the initial hyper-polarizability (β_{total}), isotropic polarizability (α_{total}), and electric dipole moment (μ_{total}).

Table 5 NLO properties of CHT

Parameter	Value	Parameter	Value
μ_x	-2.9521	β_{xxx}	-79.6445
μ_y	-1.9874	β_{xxy}	-58.0639
μ_z	1.2670	β_{xyy}	-55.7888
μ_{total}	3.7776	β_{xzz}	4570.789
α_{xx}	56.2603	β_{yyy}	117.6664
α_{xy}	-1.7106	β_{yzz}	-34.1448
α_{yy}	67.8829	β_{yxx}	215.0817
α_{xz}	-0.0291	β_{zzz}	59.11159
α_{yz}	3.8272	β_{zyy}	-8.97385
α_{zz}	15.7599	β_{zxx}	72.12976

α_{total}	$4.66x10^{-24}$	β_{total}	$3.84x10^{-30}$

According to Table 5 the first-order hyperpolarizability (β_{total}), mean polarizabilities (α_{total}), and the overall dipole moment (μ_{total}) of CHT are $3.84x10^{-30}$ esu, $4.66x10^{-24}$ esu, and 3.7776 Debye, respectively. Dipole moment of CHT is 1.016 times greater than that of urea (3.83 Debye) and 1.43 times greater than KDP crystal (5.4 Debye). The first-order hyperpolarizability of CHT is 6.1637 times higher than for urea ($0.6230x10^{-30}$ esu) and the outcomes demonstrate CHT's suitability for NLO applications.

3.6.2 Photo-catalytic Dye Degradation

The photodegradation of malachite green dye under UV light was used to assess the photocatalytic activity of CHT-nanoparticles. The absorbance of the MG solution was measured at various time intervals in order to assess the photocatalytic activity. According to the findings shown in Fig. 9, CHT demonstrated photocatalytic degradation efficiency of 78% towards malachite green dye.

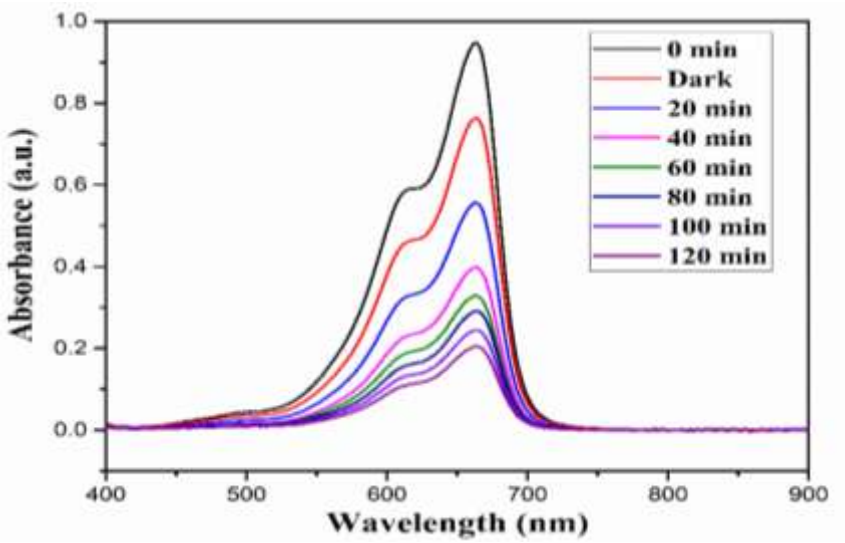

Fig. 9 Photo catalytic degradation plot of MG dye using CHT

CONCLUSION

Using the reflux approach, new surface-modified metal chloride-ligand-TiO2 nanoparticles were effectively created, and PXRD, FT-IR, FT-Raman, and UV-visible spectroscopy were used to characterize them. PXRD reveals crystalline, sharp peaks on anatase TiO2 nanopaticles together with the presence of metal chloride. The DFT/B3PW91/LANL2DZ basis set was used for structural optimization, and NCA was used to interpret the vibrational modes. Metal chloride substitution is the cause of the red shift in the C=O vibration mode. FMO was used to determine the band gap energy, and MEP was used to render the reactive sites. CHT's total dipole moment is 1.43 times larger than that of KDP crystal and 1.016 times larger than that of urea. Its first-order hyperpolarizability is 6.1637 times greater than that of urea and the result show that CHT is suitable for NLO applications. Malachite Green dye was photo-catalytically destroyed by UV light, and in just 120 minutes, CHT broke down 78% of the dye.

Acknowledgement

The author's thank Dr. I. Hubert Joe, Associate Professor in Department of Physics, Kerala University for granting us permission to do computational works in their Research Lab and The Sophisticated Analytical Instruments Facility (SAIF), IIT Chennai for recording FT-Raman Spectra.

Declaration of Compliance with Ethical Standards

The authors confirm that this manuscript is original, has not been published previously, and is not currently under consideration for publication.

Declaration of competing interest

The authors declare that they have no known competing financial interests or personal relationships that could have appeared to influence the work reported in this paper.

Declaration of Funding

The authors declare that they have no funding information to disclose.

Data Availability Statement

The data presented in this study are available upon request.

Author Contribution

Conceptualization, Formal analysis and investigation, Writing - original draft preparation: **R. S. Bemina**
Writing - review and editing, Supervision: **T. Joselin Beaula**

REFERENCE

[1] M. Hoang, J. Bae, J. Hur, Applied Surface Science on surface-modified TiO 2 nanoparticles, Appl. Surf. Sci. 604 (2022) 154528. https://doi.org/10.1016/j.apsusc.2022.154528.
[2] J. Chen, X. Li, Y. Li, Y. Li, Y. Du, S. Li, R. Wang, Y. Yang, Y. Liu, Enhanced bioelectrochemical performance of CoS2/TiO2 attaching Fe-based metal organic frameworks grown on NiFe-layered double hydroxide as cathode catalyst in microbial fuel cell, Int. J. Hydrogen Energy 72 (2024) 124–132. https://doi.org/10.1016/j.ijhydene.2024.05.389.
[3] H. Kaur, A. Kalia, J.S. Sandhu, G.S. Dheri, G. Kaur, S. Pathania, Interaction of TiO2 nanoparticles with soil: Effect on microbiological and chemical traits, Chemosphere 301 (2022) 134629. https://doi.org/10.1016/j.chemosphere.2022.134629.
[4] S. Rajendran, X. Arulantham, P. Pitchai, S. Sundarajan, Metal (II) complexes with derived from 3-hydroxy-2-(3-nitrophenyl)-4H-chromen-4-one; synthesis and photocatalytic activity, J. Mater. Sci. Mater. Electron. 30 (2019) 6669–6679. https://doi.org/10.1007/s10854-019-00976-z.
[5] R. Ben Mammar, L. Hamadou, Highly broadband plasmonic Pt nanoparticles modified α -Fe 2 O 3 / TiO 2 nanotubes for efficient photoelectrochemical water splitting, Opt. Mater. (Amst). 143 (2023) 114191. https://doi.org/10.1016/j.optmat.2023.114191.
[6] S. Jiao, M. Shang, Y. Chen, G. Pang, In situ noble metal-ion modified TiO2 rutile nanobars with highly exposed {110} facets: Synthesis, structure, and catalytic properties, Colloids Interface Sci. Commun. 58 (2024) 100761. https://doi.org/10.1016/j.colcom.2023.100761.
[7] Z. Ghasemi, A. Mohammadi, Sensitive and selective colorimetric detection of Cu (II) in water samples by thiazolylazopyrimidine-functionalized TiO2 nanoparticles, Spectrochim. Acta - Part A Mol. Biomol. Spectrosc. 239 (2020) 118554. https://doi.org/10.1016/j.saa.2020.118554.
[8] D.N. Sredojević, T. Kovač, E. Džunuzović, V. Đorđević, B.N. Grgur, J.M. Nedeljković, Surface-modified TiO2 powders with phenol derivatives: A comparative DFT and experimental study, Chem. Phys. Lett. 686 (2017) 167–172. https://doi.org/10.1016/j.cplett.2017.08.023.
[9] S. Zhao, H. Choe, S. Saqlain, C.C. Hwang, Z. Liu, Y. Choi, Z. Peng, Y.D. Kim, Simultaneous oxidation of NO and acetaldehyde over bare and Fe-modified TiO2 under visible light irradiation, Appl. Surf. Sci. 627 (2023) 157308. https://doi.org/10.1016/j.apsusc.2023.157308.
[10] R. Amiri, A. Bourezgui, W. Djeridi, F. Dappozze, A. Houas, C. Guillard, L. Elsellami, Surface modification of TiO2 with a less expensive metal (iron) to exploit solar energy in photocatalysis: An ecological and economical solution, Int. J. Hydrogen Energy 51 (2024) 638–647. https://doi.org/10.1016/j.ijhydene.2023.08.283.
[11] T. Georgakopoulos, N. Todorova, S. Karapati, K. Pomoni, C. Trapalis, Materials Science in Semiconductor Processing Photoconductivity studies on surface modified TiO 2 nanoparticles, Mater. Sci. Semicond. Process. 99 (2019) 175–181. https://doi.org/10.1016/j.mssp.2019.04.027.
[12] B. Yan, G. Chen, B. Ma, Y. Guo, Y. Zha, J. Li, S. Wang, J. Liu, B. Zhao, H. Xie, Construction of surface plasmonic Bi nanoparticles and α-Bi2O3 co-modified TiO2 nanotube arrays for enhanced photocatalytic degradation of ciprofloxacin: Performance, DFT calculation and mechanism, Sep. Purif. Technol. 330 (2024) 125180. https://doi.org/10.1016/j.seppur.2023.125180.
[13] C. Diaz-Uribe, F. Duran, W. Vallejo, E. Puello, X. Zarate, E. Schott, Photocatalytic study of TiO2 thin films modified with Anderson-type polyoxometalates (Cr, Co and Ni): Experimental and DFT study, Polyhedron 231 (2023) 116253. https://doi.org/10.1016/j.poly.2022.116253.
[14] X. Mu, Q. Xu, Y. Xie, Y. Ma, Z. Zhang, Z. Shen, Y. Guo, J. Yu, S. Ajmal, W. Zhang, J. Zhao, Hollow cubic TiO2 loaded with copper and gold nanoparticles for photocatalytic CO2 reduction, J. Alloys Compd. 980 (2024) 173589. https://doi.org/10.1016/j.jallcom.2024.173589.
[15] Z. Barbieriková, D. Dvoranová, V. Brezová, E. Džunuzović, D.N. Sredojević, V. Lazić, J.M. Nedeljković, Visible-light-responsive surface-modified TiO2 powder with 4-chlorophenol: A combined experimental and DFT study, Opt. Mater. (Amst). 89 (2019) 237–242. https://doi.org/10.1016/j.optmat.2019.01.027.
[16] A.T. Amigun, F.A. Adekola, J.O. Tijani, S. Mustapha, Photocatalytic degradation of malachite green dye using nitrogen/sodium/iron-TiO2 nanocatalysts, Results Chem. 4 (2022) 100480. https://doi.org/10.1016/j.rechem.2022.100480.
[17] A. Bokare, M. Pai, A.A. Athawale, Surface modified Nd doped TiO 2 nanoparticles as photocatalysts in UV and solar light irradiation, Sol. Energy 91 (2013) 111–119. https://doi.org/10.1016/j.solener.2013.02.005.
[18] M. Jiang, K. Yang, Y. Liu, L. Yao, Density functional theory of NO2 and N2O adsorption on the transition metal modified TiO2 surface, Chem. Phys. Lett. 834 (2024) 140977. https://doi.org/10.1016/j.cplett.2023.140977.
[19] V.T. Lukong, C.N. Chukwuati, G. Enebe, O.R. Onisuru, K. Ukoba, T.C. Jen, The development and application of Cu@TiO2@SAPO-34 as better photocatalyst towards degradation of various pollutants, Environ. Technol. Innov. 35 (2024) 103700. https://doi.org/10.1016/j.eti.2024.103700.
[20] G. Zhang, Y. Jiang, Z. Yang, X. Sun, Y. Xu, S. Cheng, X. Zhang, J. Song, The regulation mechanism of transition metal doping on Hg0 adsorption and oxidation on Ce/TiO2(001) surface: A DFT study, Sci. Total Environ. 927 (2024) 172334.

https://doi.org/10.1016/j.scitotenv.2024.172334.
[21] L. Sun, Z. Zhou, Y. Wu, Z. Meng, H. Huang, T. Li, Z. Wang, Y. Yang, A novel colormetric and light-up fluorescent sensor from flavonol derivative grafted cellulose for rapid and sensitive detection of Hg2+ and its applications in biological and environmental system, Int. J. Biol. Macromol. 266 (2024) 131209. https://doi.org/10.1016/j.ijbiomac.2024.131209.
[22] Z. Sroka, B. Żbikowska, J. Hładyszowski, The antiradical activity of some selected flavones and flavonols. Experimental and quantum mechanical study, J. Mol. Model. 21 (2015). https://doi.org/10.1007/s00894-015-2848-1.
[23] W. Xiao, Q. Zhang, D.H. You, N.B. Li, G.M. Zhou, H.Q. Luo, Construction of a novel flavonol fluorescent probe for copper (II) ion detection and its application in actual samples, Spectrochim. Acta - Part A Mol. Biomol. Spectrosc. 314 (2024) 124175. https://doi.org/10.1016/j.saa.2024.124175.
[24] M.J. Frisch, G.W. Trucks, H.B. Schlegel, G.E. Scuseria, M.A. Robb, J.R. Cheeseman, G. Scalmani, V. Barone, B. Mennucci, G.A. Petersson, H. Nakatsuji, M. Caricato, X. Li, H.P. Hratchian, A.F. Izmaylov, J. Bloino, G. Zheng, J.L. Sonnenberg, M. Hada, M. Ehara, K. Toyota, R. Fukuda, J. Hasegawa, M. Ishida, T. Nakajima, Y. Honda, O. Kitao, H. Nakai, T. Vreven, J.A. Montgomery, J.E. Peralta, F. Ogliaro, M. Bearpark, J.J. Heyd, E. Brothers, K.N. Kudin, V.N. Staroverov, R. Kobayashi, J. Normand, K. Raghavachari, A. Rendell, J.C. Burant, S.S. Iyengar, J. Tomasi, M. Cossi, N. Rega, J.M. Millam, M. Klene, J.E. Knox, J.B. Cross, V. Bakken, C. Adamo, J. Jaramillo, R. Gomperts, R.E. Stratmann, O. Yazyev, A.J. Austin, R. Cammi, C. Pomelli, J.W. Ochterski, R.L. Martin, K. Morokuma, V.G. Zakrzewski, G.A. Voth, P. Salvador, J.J. Dannenberg, S. Dapprich, A.D. Daniels, Farkas, J.B. Foresman, J. V Ortiz, J. Cioslowski, D.J. Fox, Gaussian 09, Revision B.01, Gaussian 09, Revis. B.01, Gaussian, Inc., Wallingford CT (2009) 1–20.
[25] R. Dennington, T. Keith, J. Millam,GaussView, Version 5, Semichem Inc., Shawnee Mission, KS, 2009.
[26] A.T. Dana, Effect of CuCl2 powder on the optical characterization of Methylcellulose (MC) polymer composite, Alexandria Eng. J. 61 (2022) 2354–2365. https://doi.org/10.1016/j.aej.2021.06.088.
[27] M. Saravanakumar, J. Chandrasekaran, M. Krishnakumar, B. Babu, B. Mohanbabu, G. Vinitha, Growth, spectral and quantum chemical investigation on hexamethylenetetramine 4-nitrophenol monohydrate single crystals for second harmonic generation and optical limiting applications, J. Mol. Struct. 1265 (2022) 133406. https://doi.org/10.1016/j.molstruc.2022.133406.
[28] G. Vijayalakshmi, J.I. Jeyamalar, J.J. Kores, J. Shakina, B.R.D. Nayagam, Synthesis, Spectroscopic Characterization, Molecular Docking, Quantum Chemical Studies, Topological Analysis (RDG, ELF, LOL), and Evalubation of Antibacterial and Anticancer Activities of Thiomorpholinium 4-Nitrobenzoate Crystalline Salt, J. Mol. Struct. (2025) 142438. https://doi.org/10.1016/j.molstruc.2025.142438.
[29] C.S. Abraham, S. Muthu, J.C. Prasana, B. Fathima Rizwana, S. Armaković, S.J. Armaković, Vibrational and electronic absorption spectroscopic profiling, natural hybrid orbital, charge transfer, electron localization function and molecular docking analysis on 3-amino-3-(2-nitrophenyl) propionic acid, J. Mol. Struct. 1171 (2018) 733–746. https://doi.org/10.1016/j.molstruc.2018.06.057.
[30] F. Ullah, U. Ghani, M.S. Mohamed Saheed, A PN-type CuO@TiO2 nanorods heterojunction for efficient PEC water splitting: DFT model and experimental investigation on the effect of calcination temperature, Int. J. Hydrogen Energy 48 (2023) 39866–39884. https://doi.org/10.1016/j.ijhydene.2023.07.159.
[31] T. Ohsaka, F. Izumi, Y. Fujiki, Raman spectrum of anatase, TiO2, J. Raman Spectrosc. 7 (1978) 321–324. https://doi.org/10.1002/jrs.1250070606.
[32] H. Gökce, S. Bahçeli, G. Alpaslan, Structural, vibrational, electronic, NLO and molecular docking analyses of two novel Cu(II) and Pd(II) complexes with pyridine and oxadiazole coordination, Inorg. Chem. Commun. 168 (2024). https://doi.org/10.1016/j.inoche.2024.112852.
[33] A.D. Steffy, D.A. Dhas, I.H. Joe, B. Gunasekaran, G. Vinitha, Crystal growth and vibrational spectroscopic studies on the novel nlo active piperazine-1,4-diium 3-phenyl-2-propenoate single crystal by experimental and computational technique, J. Mol. Struct. 1287 (2023) 135655. https://doi.org/10.1016/j.molstruc.2023.135655.
[34] J.D. Deephlin Tarika, A. Rathika, A. Arun kumar, X.D. Divya Dexlin, D. Deva Jayanthi, T. Joselin Beaula, Consequence of Proton Transfer and Hydrogen Bonding Interactions on the Molecular, Vibrational and Biological properties of the Novelly Synthesized Antibacterial Compound bis-(4-Dimethylaminopyridinium) bis-(3, 5-Dinitrobenzoate) monohydrate using DFT Stu, J. Mol. Struct. 1261 (2022) 132914. https://doi.org/10.1016/j.molstruc.2022.132914.
[35] C. Charanya, S. Sampathkrishnan, N. Balamurugan, Quantum Chemical Computations, Molecular Docking, Vibrational Spectroscopic Analysis, Non-Linear Optical Properties and DFT Calculation of 2-[(2,3-Dimethylphenyl)Amino]Benzoic Acid, Polycycl. Aromat. Compd. 41 (2021) 1813–1834. https://doi.org/10.1080/10406638.2019.1700138.
[36] Y.S. Mary, C. Yohannan Panicker, H.T. Varghese, K. Raju, T.E. Bolelli, I. Yildiz, C.M. Granadeiro, H.I.S. Nogueira, Vibrational spectroscopic studies and computational study of 4-fluoro-N-(2′-hydroxy-4′-nitrophenyl)phenylacetamide, J. Mol. Struct. 994 (2011) 223–231. https://doi.org/10.1016/j.molstruc.2011.03.022.
[37] H.M. Robert, D. Usha, M. Amalanathan, R.R.J. Geetha, M.S.M. Mary, Vibrational spectral, density functional theory and molecular docking analysis on 4-nitrobenzohydrazide, J. Mol. Struct. 1223 (2020) 128948. https://doi.org/10.1016/j.molstruc.2020.128948.
[38] S.B. Bukhari, S. Memon, M. Mahroof-Tahir, M.I. Bhanger, Synthesis, characterization and antioxidant activity copper-quercetin complex, Spectrochim. Acta - Part A Mol. Biomol. Spectrosc. 71 (2009) 1901–1906. https://doi.org/10.1016/j.saa.2008.07.030.
[39] T. Sivaranajani, T. Jayavarthanan, S. Suresh, C.S. Biju, A. Jayanthi, L. Sangeetha, C. Saveetha, A.A.P. Frit, M. Muruganandam, Vibrational spectra and quantum chemical investigations on nicotinium nitrate monohydrate single crystal for anti bacterial studies, Chem. Phys. Impact 6 (2023) 100200. https://doi.org/10.1016/j.chphi.2023.100200.

[40] X.D.D. Dexlin, J.D.D. Tarika, M. Sethuram, T.J. Beaula, Synthesis , vibrational Depictions , IRI interpretations and docking research on coordination metal complex Diaqua aspartato zinc (II) monohydrate using DFT approach, J. Mol. Liq. 351 (2022) 118687. https://doi.org/10.1016/j.molliq.2022.118687.

[41] S. Manikandan, T. Sundareswaran, K. Jayamoorthy, G. Sasikumar, Investigation on Hirshfeld surface analysis, molecular geometry, DFT, MEP, and molecular docking analysis on benzotriazole oxalate against SARS-CoV-2 virus, J. Mol. Struct. 1316 (2024) 138961. https://doi.org/10.1016/j.molstruc.2024.138961.

[42] M. Lawrence, P. Rajesh, A. Saral, T.C. Jeyakumar, N.S. Alharbi, G. Abbas, S. Muthu, Solute solvent interaction study on 9,9-dihydroxynanoic acid by DFT, IR, Raman, UV, MEP, quantum parameters and docking studies, J. Mol. Liq. 397 (2024) 124053. https://doi.org/10.1016/j.molliq.2024.124053.

[43] R. Bhavani, S. Elangovan, G. Suresh, S. Sankar, N. Kanagathara, P. Revathi, Molecular structure, optical, first-order hyper polarizability, electronic properties, reactivity (ELF and LOL) — computational analysis using DFT and Multiwfn for 2, 3-diaminopyridinium selenate, Inorg. Chem. Commun. 165 (2024) 112584. https://doi.org/10.1016/j.inoche.2024.112584.